Dielectric approaches for interactions of protons, positrons, and electrons in cold matter and plasmas

C. D. Archubi [*], C. C. Montanari [†], and N. R. Arista[‡]

Instituto de Astronomía y Física del Espacio, Universidad de Buenos Aires, Consejo Nacional de Investigaciones Científicas y Técnicas, Ciudad Universitaria, 1428 Buenos Aires, Argentina
and Centro Atómico Bariloche and Instituto Balseiro, and Comisión Nacional de Energía Atómica, 8400 S. C. de Bariloche, Argentina

This work investigates the projectile and temperature dependence of the energy loss of charged particles in matter. To this end, we analyze two dielectric approaches which consider the presence of bound and free electrons and the effects of the ionization process. With these approaches, we calculate the energy-loss moments of protons, positrons, and electrons traversing Si, Fe, and Al targets, both in the cold solid phase and in the plasma state. We compare the results from the unified-wave-packet model (UWPM) and the shellwise local plasma approximation (SLPA) on an extensive range of parameters, including low, intermediate, and high projectile energies and target temperatures going from cold solid-state densities to hot plasma with temperatures up to 1000 eV. We reformulate the SLPA to include light-particle restrictions. We give special consideration to the case of positrons and electrons, where the inner-shell effects have not been analyzed in our previous works. Comparisons with experimental results for cold solid targets are presented, and stopping enhancement effects for heated targets are described, showing the physical origin of these effects.

I. INTRODUCTION

Particle-plasma interactions are of central interest in plasma heating by injection of neutral beams in Tokamak devices, by alpha particles produced in nuclear fusion reactors, in inertial-confinement-fusion studies, and also to describe processes that take place in astrophysical plasmas [1–3]. Particularly, elements such as iron and carbon are related to fusion reactor walls and, together with silicon, are of interest in astrophysical research. Thus, studying the energy loss of heavy and light particles traversing different targets at high temperatures has attracted great interest in the last decades [4–13].

Positron studies also bear great interest in astrophysics, including studies of stellar opacities and positron processes in stars, in particular in the sun, where positrons are created both in the proton-proton chain reaction and in the C-N-O cycle [3,14]. In a different area of research, studies of positron penetration and annihilation in solids are of great interest in materials science (mostly through angular correlations and positron lifetime studies). These studies provide much information on crystalline and surface structures and the behavior of impurities and vacancies in different materials [15–17].

On the other hand, theoretical and experimental research regarding the energy loss by electrons and positrons in heated solids and plasmas is quite scarce compared to ion beams. A pioneering and comprehensive study was made

by Ritchie [18], showing the differences between electrons, positrons, and heavy particles in a free electron gas at zero temperature and obtaining analytical expressions for low and high energies. Experimental measurements were done by several researchers for electrons [19–30] and positrons [31–35] in cold media, and standard theoretical approaches were developed long ago [36,37]. Recently a combination of semiempirical dielectric functions and optical oscillator strength (OOS) was used with good results [38–41], also for cold solid targets. However, a full-theoretical method capable of giving an account of the different energy-loss moments for light particles in hot targets in a wide range of projectile energies has not been addressed up to now.

In recent works, we developed a complete study of statistical and temperature effects on the interactions and energy-loss moments (ELMs) of protons [12] and light particles (positrons and electrons) [13] in a hot free electron gas. However, calculating the total ELMs for positrons and electrons in plasma media, including the effects of inner shells, is still a pending and open problem. Hence, the purpose of the present work is to present theoretical developments to describe the total ELM of heavy and light projectiles, including the contributions of target-bound electrons and the temperature effects. We propose two different approaches to address this issue: the unified-wave-packet model (UWPM) and the shellwise local plasma approximation (SLPA). We will also refer to the so-called plasma-wave-packet model (PWPM), which is a restricted version of the UWPM that applies only to the free-electron plasma [13]. We analyze the projectile dependence by considering protons, positrons, and electrons, as well as temperature effects at high velocities for all the considered projectiles. We calculate the free-electron-gas (FEG)

*archubi@iafe.uba.ar
†mclaudia@iafe.uba.ar
‡arista@cab.cnea.ar

contribution by using the PWPM [13], based on Gaussian wave functions within a quantum formulation [42–45]. Finally, we calculate the total ELM by adding both contributions: SLPA or UWPM for the inner shells and the PWPM result for the FEG.

This work is organized as follows: Sec. II shows a brief review of UWPM and SLPA methods to calculate inner-shell contributions to the ELM, paying special attention to light-particle restrictions; Sec. III revisits the treatment for the two kinds of excitations, individual and collective, according to the UWPM method for a FEG; Sec. IV shows the UWPM and SLPA results for the different ELMs of protons, positrons, and electrons traversing cold targets and comparisons with available experimental data. A special discussion about the role of inner shells in the different moments is presented. In this section, we also show the UWPM and SLPA results considering the temperature effect for a Si target. Finally, Sec. V presents the summary and conclusions. A detailed analysis of the ionization effect for hot targets is performed in the Appendix. Atomic units are used unless other units are explicitly mentioned.

II. INNER SHELLS CONTRIBUTION AT FINITE TEMPERATURES

In what follows, we calculate the inner-shell contribution to the energy-loss moment of order s, $Q^{(s)}$, by adding independent contributions $Q_i^{(s)}$ of the different i subshells. The temperature effect is incorporated considering the population of the different shells according to the ionization degree of the target. In this work, we use the results from FLYCHK code [46] to obtain the ionization degree of the target as a function of the temperature T. At the same time, we depopulate gradually from outside to inside the electronic shells. The free electron gas density is incremented by adding the ionized electrons. Finally, we sum the different contributions of the inner shells weighted by the remaining electrons in the corresponding shells. The total moment of the energy-loss distribution is

$$Q^{(s)}(T) = \Sigma_i W_i(T) Q_i^{(s)}, \qquad (1)$$

with W_i being the weight value corresponding to the population of the partially ionized i-shell at temperature T, and s represents the different orders of the energy loss. For cold targets, $W_i(T) = 1$ for all the occupied shells. This expression represents in a compact way the three main moments of the energy loss to be considered here, namely, the inverse mean-free path $\Lambda^{-1} = Q^{(0)}$, stopping power $S = Q^{(1)}$, and straggling parameter $\Omega = [Q^{(2)}]^{1/2}$, which correspond to the cases $s = 0$, 1, and 2, respectively.

A. UWPM formulation

The UWPM [12] is a many-electron model that extends Kaneko formalism [42–44] to account for temperature effects and inner-shell contributions to the energy loss for protons and heavy ions. Briefly, in Kaneko's proposal, the dielectric response function is calculated assuming a Gaussian wave packet for target electrons. Using appropriate Gaussian parameters, electronic wave functions consistent with Hartree-Fock formulation in the momentum space are

obtained. Consequently, an alternative dielectric response function is obtained using linear response theory similarly to the original Lindhard method [37].

Within the UWPM, the inner-shell contributions are calculated keeping the original Kaneko parameters, incorporating the binding energy of each shell, and considering temperature effects according to Eq. (1). We generalize our original UWPM method [12] for the impact of heavy and light projectiles. The energy loss of a projectile of mass m_P, charge Z_P, and impact velocity v due to the individual excitations of target electrons of the i-shell can be expressed in a unified way by

$$Q_i^{(s)} = \frac{2}{\pi} \frac{Z_P^2}{v^2} \int_0^{q_{max}} F_i^{(s)}(q) \, g_x(q) \frac{dq}{q}. \qquad (2)$$

This extension is assured by integrating the momentum transferred q in Eq. (2) up to $q_{max} = 2m_P v$. It is worth remarking that for protons and heavier particles $q_{max} \sim \infty$, but for light projectiles (electrons and positrons), it has a finite value.

The factor $g_x(q)$ is crucial because it considers the exchange symmetry as a part of the identity effect in the electron-electron interaction. This term was first obtained by Ochkur [47,48] and has been largely used in inelastic electron scattering in various media since then [39–41]. It is taken as

$$g_x(q) = 1 + (q/v)^4 - (q/v)^2 \qquad (3)$$

for electron impact, and $g_x(q) = 1$ for proton and positron impact. Very detailed studies made by Hippler [49] and Shinotsuka *et al.* [50] show that the Ochkur factor considerably improves electron impact ionization and stopping power calculations.

Within the dielectric formalism, the loss function in Eq. (2) is given by

$$F_i^{(s)}(q) = \int_0^{\omega_{max}} \omega^s G(\omega) \, \mathrm{Im}\left[\frac{-1}{\varepsilon_i(q,\omega)}\right] d\omega, \qquad (4)$$

where ω is the energy loss by the impinging projectile, with the maximum value being

$$\omega_{max}(q,v) = qv - q^2/(2m_P). \qquad (5)$$

It can be noted that $\omega_{max}(q,v) = 0$ if $q = q_{max} = 2m_P v$. Therefore, Eq. (5) leads to kinematic restrictions for light particles. The term $\mathrm{Im}[-1/\varepsilon_i(q,\omega)]$ is known as energy-loss function (ELF) and carries the information on the screening and absorption properties of the plasma, equivalent to the oscillator strength distribution in the binary collisional treatment of atomic excitations [36]. As mentioned before, in the present UWPM, we employed Kaneko's dielectric function $\varepsilon_i(q,\omega)$ modified by the Levine-Louie method to take into account the binding energy of bound electrons in atomic shells [12]. The index i indicates the corresponding atomic shell.

The function $G(\omega)$ in Eq. (4) introduces the electron-electron quantum restrictions, i.e., Pauli exclusion principle for identical particles [13]. For the case of incident electrons, according to the UWPM, it is given by

$$G(\omega) = [1 - f_{FD}(E - \omega)][1 - f_{FD}(\omega - I_i)]H(E + I_i - 2\omega), \qquad (6)$$

with E being the impact energy of the incident electrons, I_i the binding energy of the target electron, f_{FD} the Fermi-Dirac

function, and $H(x)$ a Heaviside step function. Instead, for impinging positrons or heavy particles

$$G(\omega) = [1 - f_{\text{FD}}(\omega - I_i)]. \tag{7}$$

The presence of these factors may be explained as follows: Consider first an incident electron with energy $E_1 = v^2/2$, which, in a single scattering process, transfers an energy ω to a target electron bound with energy $E_2 = -I_i$; then the first electron ends up with energy $E_1' = E_1 - \omega$, while the second electron is ionized to a free state with energy $E_2' = \omega - I_i$. Therefore, the first two factors in Eq. (6) yield the probabilities that the states with energies E_1' and E_2' are unoccupied. The third factor (Heaviside function) in this equation is introduced to take into account the criterion that, after the scattering event, the electron that emerges with the highest energy is considered the new "primary" electron [51,52]. This criterion introduces a limit to the final energies E_1' and E_2' given by $E_1' > E_2'$. The cases where $E_1' < E_2'$ are taken into account by the exchange factor g_x. Hence, in the case of electrons, all the identity effects are considered by the g_x and $G(\omega)$ factors in Eqs. (2) and (3).

In the case of incident positrons, protons, or other ions, the only factor that appears is that of Eq. (7), which corresponds to the final state of the ionized target electron.

B. SLPA formulation

The SLPA [53–55] is also a many-electron model that deals with the response of bound electrons to the ion passage, collectively, as an inhomogeneous FEG with an ionization gap. This model is based on Lindhard quantum dielectric formalism, and verifies the high-energy limits, equipartition, and f-sum rules, as it is desirable [56]. Within the SLPA each i-shell of target electrons is described by a local density $\rho_i(r)$ (related to the wave function of the i-orbital) and the corresponding binding energy I_i. This ionization energy is introduced within the dielectric function using Levine-Louie's proposal [57], as shown below.

We generalized the SLPA for heavy and light projectiles using Eqs. (1)–(5) for the different energy-loss moments. Within the SLPA, the ELF in Eq. (4) is given by the spatial integration of a local one as follows:

$$\text{Im}\left[\frac{-1}{\varepsilon_i^{\text{SLPA}}(q, \omega)}\right] = \rho_a \int \text{Im}\left[\frac{-1}{\varepsilon(q, \omega, \rho_i(r), I_i)}\right] d\mathbf{r}, \tag{8}$$

with ρ_a being the atomic density of the cold target, and $\varepsilon[q, \omega, \rho_i(r), I_i]$ being the Levine-Louie dielectric function [57], which explicitly includes the binding energy I_i. This local assumption of the SLPA dielectric function is a fundamental characteristic of the model. In the present formulation of the SLPA for light particles, the function $G(\omega)$ in Eq. (4) is given by

$$G(\omega) = [1 - f_{\text{FD}}(E - \omega)]H(E + I_i - 2\omega) \tag{9}$$

for electron impact, and $G(\omega) = 1$ for proton and positron impact. The difference with the $G(\omega)$ for the UWPM formulation, Eqs. (6) and (7), relies upon the dielectric function properties for the FEG, which the SLPA locally verifies; they assure Pauli restriction for the final state of the ionized electron.

III. FEG CONTRIBUTION: INDIVIDUAL AND COLLECTIVE EXCITATIONS

The response of the conduction electrons of metals to the projectile perturbation includes two types of excitations: collective (plasmon) and individual or binary collisional excitations [6,18,37,58]. The latter represents the most important part of the energy loss for large momentum transfer q, while the collective or resonant type of excitation dominates the energy absorption for low q values [59].

In both methods, SLPA and UWPM, the FEG contribution is calculated independently of the inner shell contributions. To this end, we use the PWPM temperature-dependent procedure described in Ref. [13]. We applied it to both cold solid targets and hot plasma ones. In the next two subsections, we briefly resume this formalism.

Regarding the previous expressions in Eqs. (2)–(8), an explanatory note must be made. In the standard representation of the energy-loss process, only positive frequencies are considered (as in the previous expressions). However, in the PWPM method [13], the range of frequencies spans the whole negative and positive range of values (from $-\infty$. to $+\infty$.), where the range of negative (positive) ω values represent energy-loss (-gain) processes. For this reason, and to avoid confusion, in the following review of the PWPM, we denote with ω' the frequencies appearing in the formulation.

A. FEG individual excitations

As demonstrated in Ref. [13], the energy loss in plasma at temperature T can be expressed in a unified way in the form

$$Q_{\text{ind}}^{(s)} = \frac{2}{\pi} \frac{Z_P^2}{v^2} \left[\int_{q_c}^{q_{\max}} F_{\text{loss}}^{(s)}(q)\, g_x(q) \frac{dq}{q} + \int_{q_c}^{\infty} F_{\text{gain}}^{(s)}(q)\, g_x(q) \frac{dq}{q} \right], \tag{10}$$

where the subscript "ind" indicates that only the individual (nonresonant) excitations of the FEG are included. The two terms in Eq. (10) represent the energy-gain ($\omega' > 0$) and energy-loss ($\omega' < 0$) contributions explained in Ref. [13].

The F functions in Eq. (10) are given by

$$F_{\text{loss}}^{(s)}(q) = \int_{\omega'_{\min}}^{0} (\omega')^s N(\omega')\, G^{(1)}(\omega')\, \text{Im}\left[\frac{-1}{\varepsilon_T(q, \omega')}\right] d\omega' \tag{11}$$

and

$$F_{\text{gain}}^{(s)}(q) = \int_{\tilde{\omega}'_{\min}}^{\omega'_{\max}} (\omega')^s N(\omega')\, G^{(2)}(\omega')\, \text{Im}\left[\frac{-1}{\varepsilon_T(q, \omega')}\right] d\omega', \tag{12}$$

where $\varepsilon_T(q, \omega')$ is the temperature-dependent dielectric function for an electron plasma in thermal equilibrium and the factor $N(\omega')$ is the Bose function, which represents the thermal distribution of excitations in the plasma [60],

$$N(\omega') = \frac{1}{e^{\omega'/k_B T} - 1}, \tag{13}$$

with k_B being the Boltzmann's constant. In the present calculations, ε_T is the PWPM function obtained in Refs. [12,13].

The functions $G^{(1)}(\omega')$ and $G^{(2)}(\omega')$ in Eqs. (11) and (12) introduce the electron-electron quantum restrictions in the FEG transitions, i.e., Pauli exclusion principle and identical particles considerations. These restrictions apply only to incident electrons and are specified by Eqs. (48) and (49) of Ref. [13]. For other types of particles, those restrictions disappear, i.e., $G^{(1)}(\omega') = G^{(2)}(\omega') = 1$.

The limits of integration in Eqs. (11) and (12) are the following:

$$\omega'_{\min}(q, v) = -qv + q^2/(2m_P), \qquad (14)$$

$$\omega'_{\max}(q, v) = qv + q^2/(2m_P). \qquad (15)$$

Additionally, in Eq. (12) we have introduced a lower limit $\widetilde{\omega}'_{\min}$ given by

$$\widetilde{\omega}'_{\min}(q, v) = \begin{cases} 0, & q < q_{\max} \\ \omega'_{\min}(q, v), & q > q_{\max} \end{cases} \qquad (16)$$

It is clear that for heavy projectiles, $q_{\max} \sim \infty$ and $\widetilde{\omega}'_{\min} = 0$. For further information about the different values for the extremes of the q and ω integrals, see Ref. [13].

B. FEG collective excitations

The energy loss due to collective excitations of the FEG was approximated as follows: first, we isolate the plasmon contribution to the ELF [61]:

$$\text{Im}\left[\frac{-1}{\varepsilon(q, \omega')}\right] = \frac{\pi}{D(q)}[\delta(\omega' - \omega'_q) - \delta(\omega' + \omega'_q)], \qquad (17)$$

with

$$D(q) = \left|\frac{\partial \varepsilon_1(q, \omega')}{\partial \omega'}\right|_{\omega' = \omega'_q} \qquad (18)$$

and ω'_q being the frequency values along the resonance line, being $\varepsilon = \varepsilon_1 + i\varepsilon_2$.

Then, we introduce Eq. (17) in the energy-loss integrals of Eq. (10), obtaining

$$Q^{(s)}_{pl} = 2\frac{Z_P^2}{v^2}\left[(-1)^{s+1}\int_{q^{(1)}_{\min}}^{q_c}\frac{dq}{q}\frac{(\omega'_q)^s}{D(q)}N(-\omega'_q)\right.$$
$$\left. + \int_{q^{(2)}_{\min}}^{q_c}\frac{dq}{q}\frac{(\omega'_q)^s}{D(q)}N(\omega'_q)\right], \qquad (19)$$

where $q_{\min}$ has two values according to the explanations given in Ref. [13].

IV. RESULTS AND DISCUSSION

In this section, we present our results analyzing three different aspects: (i) the dependence of the energy-loss moments with the mass and type of the projectiles for a Si target; (ii) the stopping power of the same projectiles in different targets (Al and Fe); and finally, (iii) the temperature effects in the energy-loss moments of protons, electrons, and positrons in cold and hot Si.

Three energy-loss moments are analyzed theoretically and compared with the available experimental data, namely,
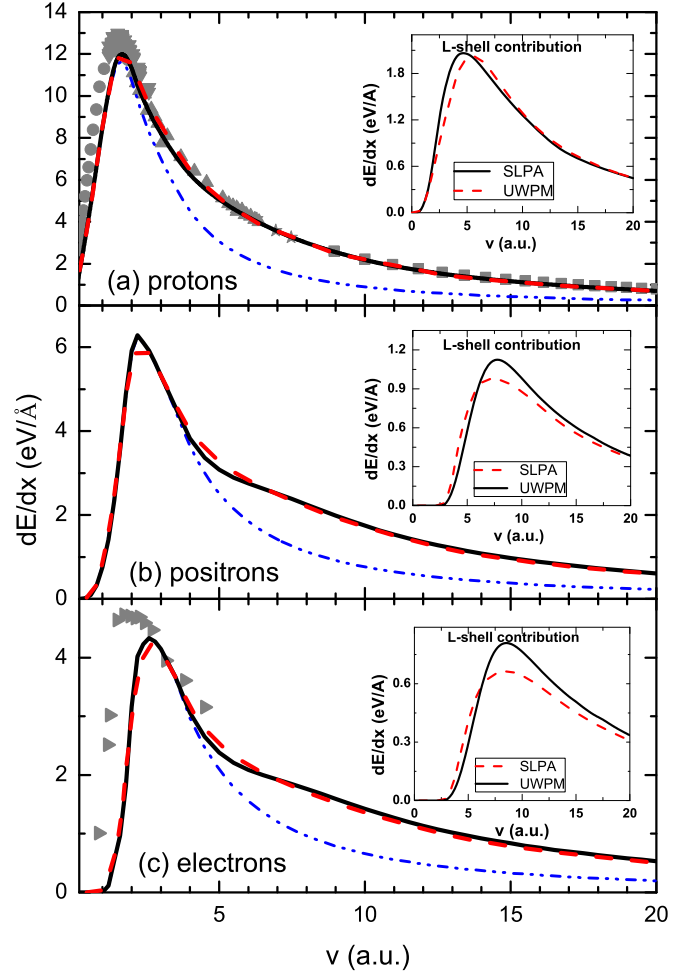

FIG. 1. Stopping power of a cold solid-state Si target for impinging (a) protons, (b) positrons, and (c) electrons as a function of the impact velocity. Curves: black-solid lines, total UWPM results (FEG + inner shells); red dashed lines, total SLPA results; blue dashed-double-dot lines, FEG contribution (PWPM). Symbols: experimental data for proton impact: circles [63], up triangles [64], down triangles [65], squares [66], and stars [67]; semiempirical values for electron impact: right-oriented triangles [27]. The inserted graphs show the results for the L-shell contribution.

stopping power ($s = 1$), energy-loss straggling ($s = 2$), and mean-free path ($s = 0$).

In what follows, we shall call "total SLPA" or "total UWPM" to the sum of the SLPA or the UWPM results for the inner shells and the PWPM results for the FEG.

A. Energy-loss moments for a Si target: Dependence on the mass and type of projectile

1. Stopping power

In Fig. 1, we display the results for the stopping of protons, positrons, and electrons traversing a cold solid Si target (density $= 4.99 \times 10^{22}$ atoms/cm^3 and $r_s = 2.01$). The results for proton impact, Fig. 1(a), show a good agreement between theoretical predictions and experimental values. Considering that the case of protons in Si is one of the most measured systems, we decided to include data since the year

2000 [62], except at high impact energies ($v > 6$) where all data are included. Both models, UWPM and SLPA, show an excellent agreement on the whole range of velocities. As expected, the difference between the total stopping power and the FEG contribution (blue dash-dot line) increases for velocities on the right side of the maximum, showing a growing influence of inner-shell contributions for higher velocities. The small insets at the right side of the figures, inside each panel, show the similarity between both treatments for the case of the L-shell contribution. It can also be observed that the SLPA results, where FEG is evaluated with UWPM dielectric function, present almost identical results to those of the full UWPM approach. This is a remarkable agreement considering the significant differences in the inner-shell calculations with both approaches. However, if we evaluate the SLPA stopping using Lindhard's dielectric function for the FEG, we should obtain a sharper maximum. This effect has been previously shown in the case of protons by Kaneko [42] and is partly because the Lindhard model produces a sharp increase in the stopping curve when the plasmon threshold is exceeded [68].

Similar results are displayed in Figs. 1(b) and 1(c) for positrons and electrons, showing a decreasing stopping behavior when the restrictions for the light particles become important, leading to the lowest maximum in the case of electrons. This is reasonable if we take into account that the electrons are the case with greater restrictions: exchange and Pauli exclusion principle due to the identity between projectile and target electrons, as well as recoil effects, Eq. (5), which apply both to electrons and positrons. The magnitude of these effects is quantified in Fig. 1: the stopping maxima for positrons and electrons are about one-half and one-third the value for protons. Differences with experimental results in the case of electrons are similar to those obtained with other theoretical approaches [39]. In this respect, it should be mentioned that the semiempirical values reported in Ref. [27] were obtained with a combination of theoretical models and measurements of energy-loss spectra taken at high energies. As discussed in Ref. [69], empirical methods to obtain electron stopping power values for energies below 100 eV ($v \sim 2.7$) should be taken cautiously. Moreover, this low-energy region is also complicated for theoretical models.

2. Mean-free path

The total mean-free path Λ is the inverse of the probability of inelastic collisions per unit path length, $\Lambda = 1/Q_{\text{Tot}}^{(0)}$, where $Q_{\text{Tot}}^{(0)} = Q_{\text{FEG}}^{(0)} + Q_{\text{shells}}^{(0)}$ is the energy-loss-distribution moment of order zero. Figure 2 displays the present results for the mean-free path of protons, electrons, and positrons in cold solid Si. As expected, the behavior of Λ is inverse to that of the stopping power (Fig. 1), i.e., the incorporation of inner-shell contributions reduces the total Λ as compared to the separate FEG results (blue dash-dotted lines in Fig. 2). As in Fig. 1, inner shell contributions become relevant for high velocities. Figure 2(c) shows the comparison of the present results with the experimental data available (only for the case of electrons). As may be seen, both UWPM and SLPA methods reproduce fairly well the behavior of the experiments, with some deviation at high energies. The insets in Fig. 2 show the
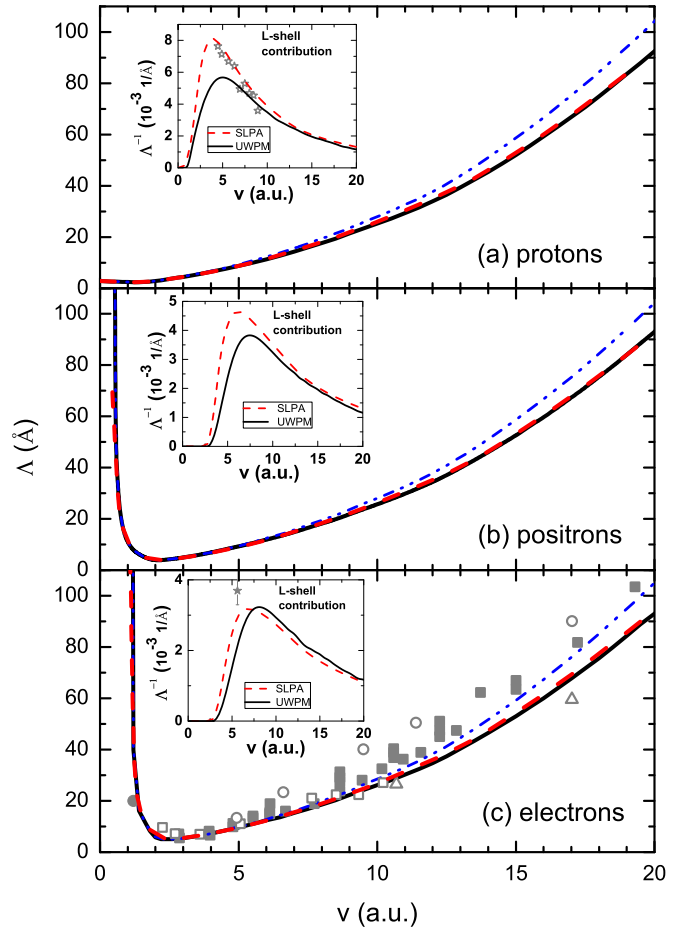

FIG. 2. Mean-free path Λ of different projectiles traversing a cold solid-state Si target as a function of projectile velocity in atomic units: (a) protons, (b) positrons, and (c) electrons. Curves: present results following the same criteria of Fig. 1. Symbols: experimental data from Ref. [23], open triangles; Ref. [24], full circles; Ref. [25], open circles; Ref. [26], open squares; Ref. [28], full squares; Ref. [70], open stars; and Ref. [71], full stars.

separate contributions of the L shell to the inverse mean-free path. Experimental data [70,71] have also been included in these insets, showing fairly good agreement with our curves for proton impact. The sharp increase of Λ for positrons and electrons at low velocities, where the FEG contribution is dominant, is due to the additional recoil and quantum restrictions, as it has been pointed out in Ref. [13].

3. Straggling

Figure 3 displays the corresponding results for the square of the energy-loss straggling Ω^2 in cold solid Si for protons, electrons, and positrons. Theoretical results are compared with available experimental data regarding proton impact. There are several measurements of electron straggling values at high energies (in the relativistic range) but very few measurements for lower energies. In particular, we did not find experimental values of electron straggling in Si targets in the range of velocities considered here. Regarding proton impact measurements, the agreement of our calculations with most of the data [73–76] is very good and within the scatter of the
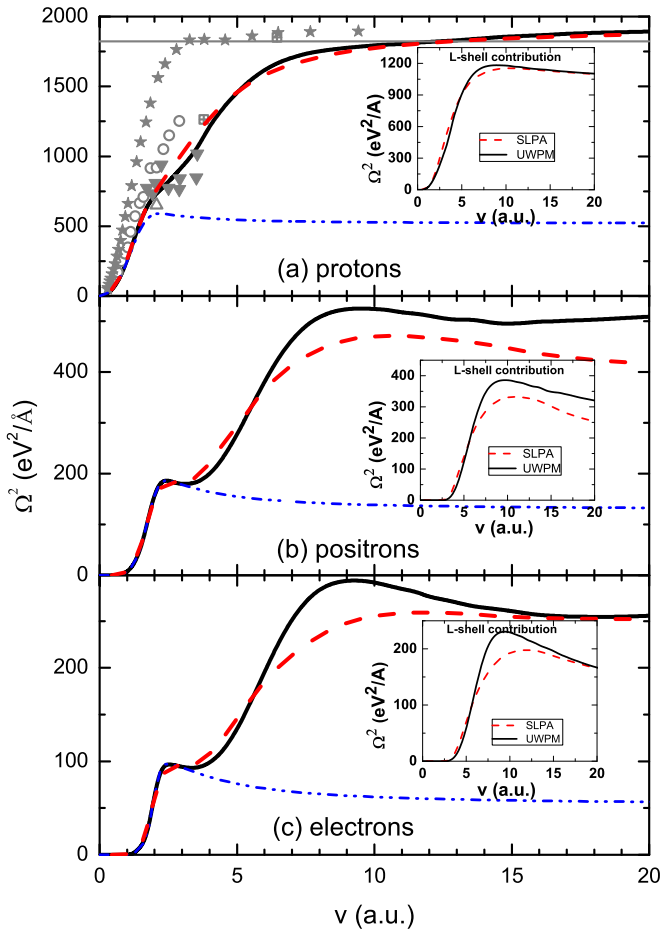
FIG. 3. Straggling parameter of cold solid-state Si target for impinging (a) protons, (b) positrons, and (c) electrons as a function of the impact velocity. Curves as in Fig. 1, with the thin horizontal line in (a) being Bohr high-energy limit. Symbols: experimental data from Ref. [72], stars; Ref. [73], open circles; Ref. [74], down triangles; Ref. [75], crossed squares; and Ref. [76], up triangles.

experimental values. It is also quite remarkable in Fig. 3 the strong disagreement of the experimental values of Ref. [72] with respect to the other measurements [73–76].

Inner shells play a major role in the energy-loss straggling, especially at high energies that are proportional to the number of electrons in each shell [77,78]. This agrees with the Bohr high-energy limit for the energy-loss straggling, proportional to the number of active electrons of each shell. Hence, a good test of the performance of the present models is the tendency to Bohr's limit at high energies, represented by the horizontal line in Fig. 3(a). Above $v = 10$ both UWPM and SLPA results match the Bohr limit very well. The high-energy limit for positrons is about four times lower than that for protons (an exact relation is shown in Ref. [61]), while the corresponding limit for electrons is still lower due to the additional restrictions.

Another point to highlight in Fig. 3 is the presence of shoulders (more notorious for light particles); a first shoulder, placed at $v \sim 2.5$, corresponds to the FEG contribution. In the case of light particles, the impact energy is much lower than for equal-velocity protons and not enough to ionize bound

electrons (ionization threshold). Then, the L-shell contribution is activated for higher velocities than for protons, as can be seen in the insets of this figure. Consequently, the shoulder is more pronounced for positrons and electrons. The $2s$ and $1s$ contributions produce a less notorious increase in the curves for higher velocities. A more detailed analysis shows that the $1s$ contribution is the reason for a slight slope change for positron and electron velocities greater than 15 a.u. Similarly to the case of stopping power, the total straggling values decrease from protons to electrons, being this decreasing behavior due to quantum restrictions and also because the maximum energy transfer for light particles is lower than for protons with equal velocities. More precisely, at high projectile velocities, the energy straggling is governed by near collisions (that is, great values of transferred momentum q), and the maximum energy transfer for light particles given by Eq. (5) produces an important reduction of the maximum momentum transfer. Thus, a drastic reduction of straggling, well below the Bohr limit, shall occur for these projectiles.

Finally, as the role of inner-shell contributions is more important in straggling, here we appreciate more clearly some differences between the results from both methods: SLPA produces lower inner-shell contributions than UWPM, as is shown in the insets of Fig. 3 for positrons and electrons. These differences, however, are rather small (almost null in the case of protons), and so both methods show, in general aspects, similar behaviors and fairly good agreements for all the moments of the energy-loss distributions.

4. Inner shells and ionization energies

To analyze more carefully the role of inner shells, we display in Fig. 4 the relative contributions of the FEG with respect to the total energy-loss moment as a function of the projectile velocity. Note that for low velocities, the entire result is produced by the FEG. However, this relative contribution drops with increasing velocities due to the increasing contribution of the inner shells.

This figure shows that, at high impact velocities, the importance of inner shells increases with the increasing order of the energy-loss moment, being more important in the straggling [a drop of $\sim$70%–80% in Fig. 4(b)] than in the stopping [$\sim$60%, Fig. 4(a)], and than in the inverse mean-free path [$\sim$10%–12%, Fig. 4(c)]. This effect can also be clearly appreciated in Figs. 1–3 by comparing the total values with those for the FEG, where the inner-shell contribution is found to be greatest for the straggling, and smallest for the mean-free path.

We also see in this figure that the rapid decrease due to the effect of inner shells appears before for protons than for the light particles. This interesting behavior is due to the particular restrictions that apply to positrons and electrons; this is the reason for the delay in the appearance of the inner-shell contributions in Fig. 1. These restrictions are of a kinematic nature for both particles [in accord with Eq. (5)] and, additionally, quantum (identity) restrictions in the case of electrons.

To get further insights into the description of inner-shell contributions in both SLPA and UWPM methods, we can make some particular comments about the role of the
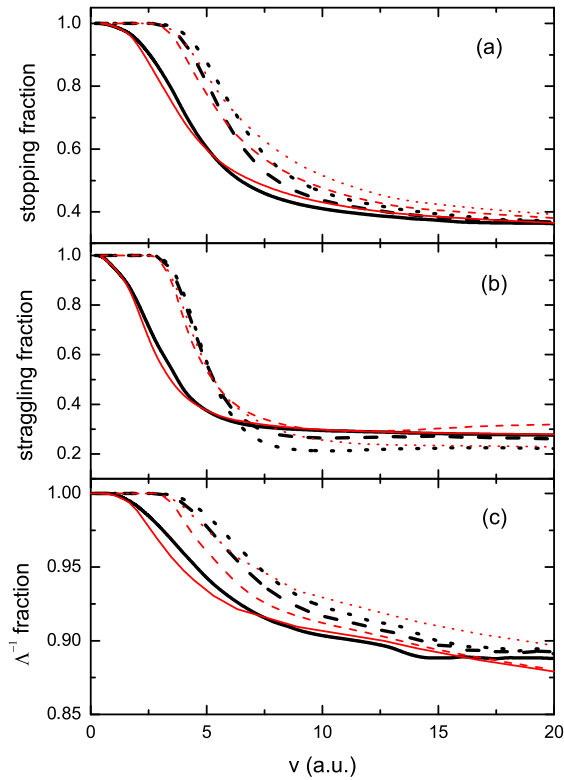
FIG. 4. Relative contribution of FEG to the total energy-loss moments of different projectiles traversing a cold-solid Si target as a function of projectile velocity: (a) stopping power, (b) straggling, and (c) inverse mean-free path. Curves: thick black curves represent UWPM values for proton (solid), positron (dash), and electron (dot) impact; thin red curves represent SLPA values for proton (solid), positron (dash), and electron (dot) impact.
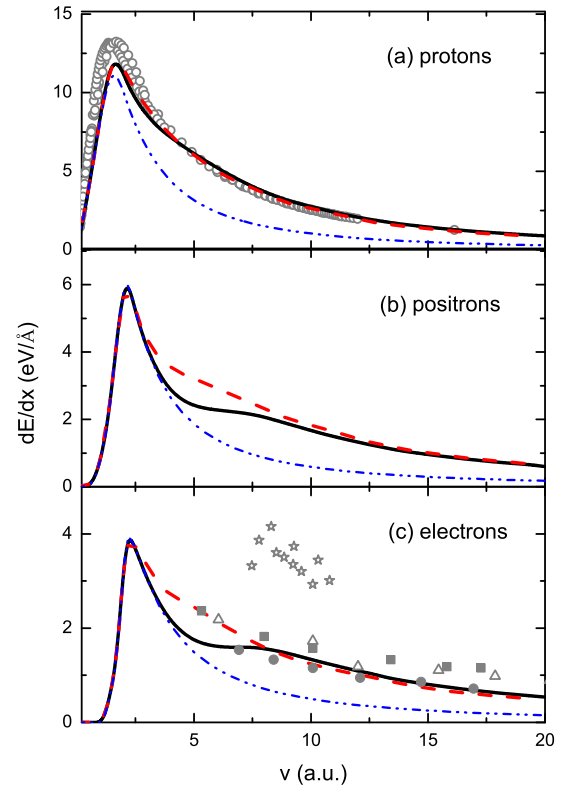

FIG. 5. Stopping power of different projectiles traversing a cold solid-state Al target as a function of projectile velocity by impinging particles: (a) protons, (b) positrons, and (c) electrons. Curves: as in Fig. 1. Symbols: experimental values; open circles, proton impact [62]; stars [19], full squares [20], full circles [21], and open triangles [22], experimental data of electrons in Al.

Levine-Louie method in both approaches. In the original wave-packet model developed by Kaneko, the target electrons are modeled by Gaussian wave-packet functions in the momentum space, which naturally contains a medium energy associated with the shell and a spread of momentum values corresponding to the Gaussian distribution. Thus, the additional quantum restrictions related to the ionization energy have a softer influence in the UWPM than in the SLPA case, where the role of the frequency cut is an essential part of the model. We also find that the influence of the gap effect in UWPM becomes lower as the order of the energy-loss moment increases, being maximum for the inverse mean-free path and minimum for the straggling. This is because, in the integrals, the energy-loss function is multiplied by different powers s of the frequency, which reduces the relative contribution of low frequencies for larger s values, and consequently softens the effect of introducing a frequency cut (via the Levine-Louie method).

B. Stopping power of different targets: Al and Fe

Figure 5 shows the present UWPM and SLPA results for the stopping powers for the different projectiles on a cold solid Al target (density $= 6.02 \times 10^{22}$ atoms/cm^3 and $r_s = 2.07$). For protons, Fig. 5(a), the UWPM and SLPA results are quite similar and agree very well with the experimental data

compiled in Ref. [62]. The stopping of protons in Al has had around 60 sets of measurements since 1949, and the dispersion of data, mainly old measurements at intermediate and low energies, messes up any theoretical-experimental comparison. We decided to include only data since 1990 for low- and
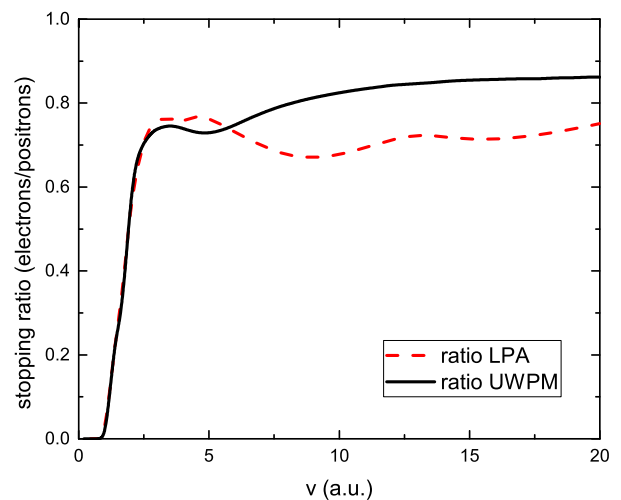

FIG. 6. Stopping power ratios of electrons and positrons traversing a cold solid-state Al as a function of projectile velocity.
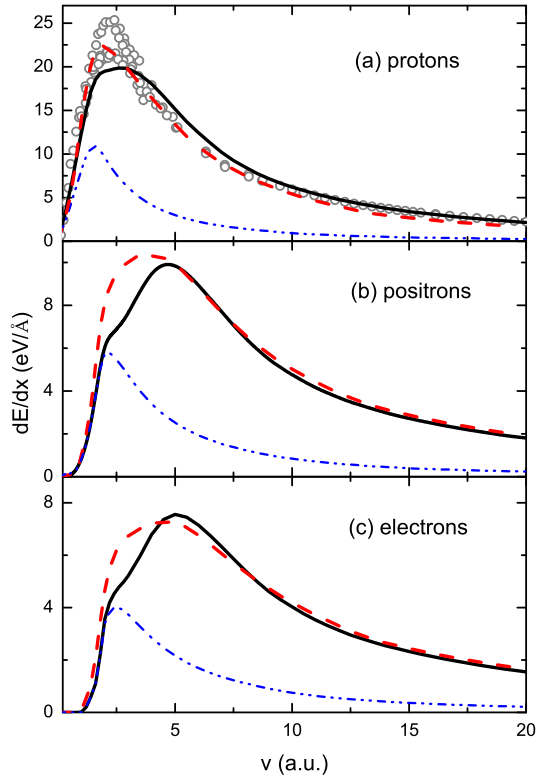
FIG. 7. Stopping power of different projectiles traversing a cold solid-state Fe as a function of projectile velocity for (a) protons, (b) positrons, and (c) electrons. Curves: as in Fig. 1. Symbols: hollow circles, a compilation of experimental data in Ref. [62].
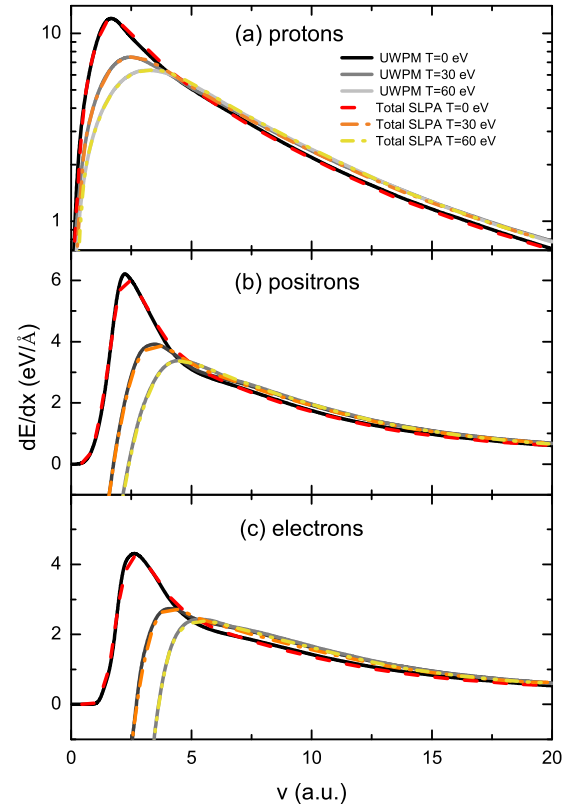

FIG. 8. Stopping power of different projectiles traversing a Si solid-state density plasma as a function of projectile velocity for different temperatures, for impinging (a) protons, (b) positrons, and (c) electrons. Curves: as indicated in the inset.

intermediate-impact energies ($v \leqslant 6$) and all the experimental data in Ref. [62] for higher-impact energies, where the spread of values is much less.

For positron and electron impact, Figs. 5(b) and 5(c), the UWPM and SLPA results show significant differences in the intermediate velocities region, i.e., $3 \leqslant v \leqslant 7$. For higher velocities, both models agree and, on average, and within the experimental uncertainties, reproduce the experimental results for electron impact reported in Refs. [20–22]. It is clear in this figure that the measurements of Ref. [19] are very different from the rest.

As already noted for Si, the comparison of the results in Figs. 5(b) and 5(c) show that the stopping power for positrons is always greater than for electrons, although tending to be closer in the high-energy limit. To highlight this conclusion, we display in Fig. 6 the ratios between the stopping powers of electrons and positrons. Our results for Al predict that the stopping of positrons is from 14% (for UWPM) to 25% (for SLPA) greater than the stopping of electrons at $v = 20$ a.u. These values are in satisfactory agreement with existing experimental results for aluminum foils that yield values of energy losses of positrons greater than those of electrons by about 15% in this range of energies [34,35].

The rest of the energy-loss moments of Al (straggling and inverse mean-free path) show similar behaviors to those previously shown for a Si target. This is understood considering the similarity of the target electronic structures. We decided not to include here the corresponding Λ and

straggling figures since they do not add significantly different information.

Another case of particular interest is that of a Fe target (density $= 8.47 \times 10^{22}$ atoms/cm^3 and $r_s = 2.118$), where the FEG contribution is comparatively much lower due to the larger number of inner-shell electrons. Figure 7 shows the behavior of the stopping power of Fe for the three different projectiles. The differences between FEG stopping (blue dashed-double dotted curves) and the total values show that here most of the energy loss is due to the contribution of inner shells at intermediate and high velocities. For proton impact, where experimental results are available, we find a reasonable agreement with the experiments, considering again the spread of experimental data around the maximum. This proves the reliability of both methods in calculating inner-shell contributions to the stopping power. In this case, the SLPA approach improves the agreement with the experiments in the region where the maximum occurs.

C. Energy loss and the temperature effect (heated solids)

The case of very hot plasmas with solid-state densities is an example of interest considering the initial stages of heated materials in inertial-confinement-fusion studies. Here we consider as a representative example a dense plasma characterized by a hot Si target at two different temperatures: 30 and 60 eV. An extension to much higher temperatures is made in the Appendix. The case considered here is, of course, an unstable
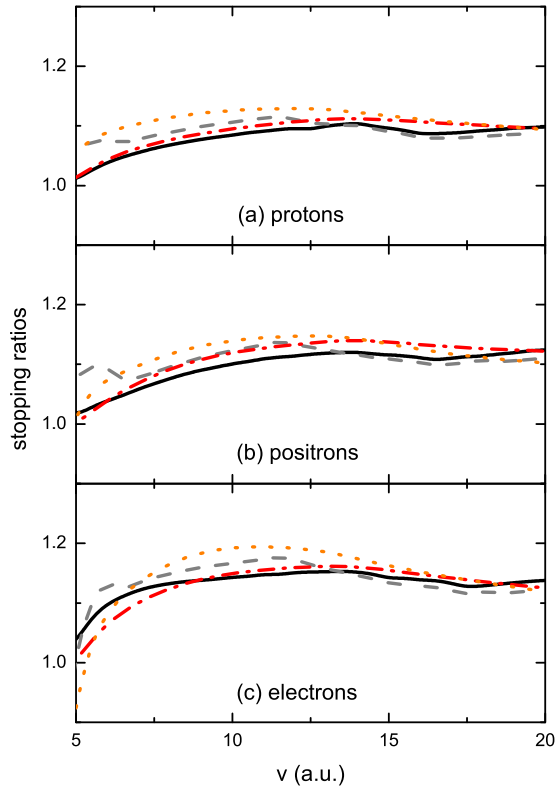
FIG. 9. Ratios of stopping powers $S(v, T)/S(v, 0)$ at $T = 30$ eV and $T = 60$ eV with respect to cold $T = 0$ values for velocities $v \geqslant 5$, for (a) protons, (b) positrons, and (c) electrons in Si. Curves: current results using UWPM for $T = 30$ eV (black solid line); UWPM for $T = 60$ eV (gray dashed line); total SLPA for $T = 30$ eV (red dash-dotted line); and total SLPA for $T = 60$ eV (orange dotted line).
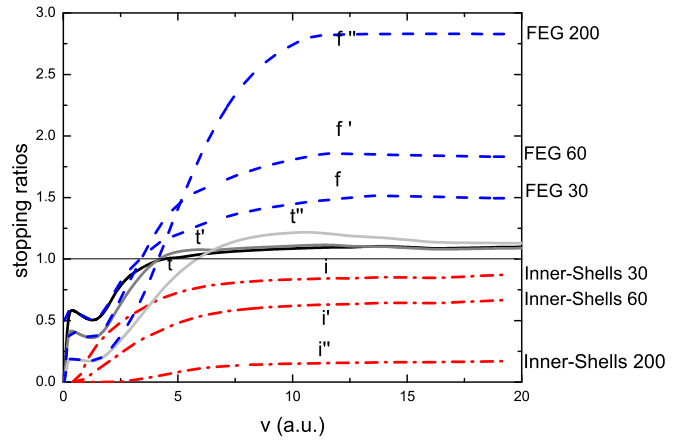

FIG. 10. UWPM ratios of the stopping power at $T = 30$ eV, $T = 60$ eV, and $T = 200$ eV with respect to cold $T = 0$ values, as a function of projectile velocity, for protons in Si. Curves f, f′, and f″: FEG stopping ratios for $T = 30/T = 0$, $T = 60/T = 0$, and $T = 200/T = 0$, respectively; curves i, i′, and i″: inner-shell stopping ratios for $T = 30/T = 0$, $T = 60/T = 0$, and $T = 200/T = 0$, respectively; curves t, t′, and t″: total stopping power ratios for the same temperatures.

system with temperatures way over the fusion point, but it pertains, for instance, to intermediate phases in an inertial confinement fusion stage. For both temperatures, the target ionization degree has been calculated with FLYCHK code [46]. The obtained number of free electrons per Si atom, N_e, for the different temperatures are $N_e = 4$ ($r_s = 2.005$) at $T = 0$, $N_e = 4.63$ ($r_s = 1.913$) for $T = 30$ eV, and $N_e = 6.06$ ($r_s = 1.746$) for $T = 60$ eV. The number of inner-shell electrons has been changed according to this, and the ionization energies of the inner shells have been shifted for each temperature according to the procedure described in Ref. [12].

Calculations of the three main energy-loss moments of protons, positrons, and electrons in hot Si are shown in Figs. 8–12. In all the cases, total values are displayed considering the addition of the inner-shell contributions (using the UWPM and the SLPA models, as explained in Sec. II) and the FEG contribution (by using the UWPM formalism as explained in Sec. III).

Figure 8 shows the temperature dependence of the stopping power. In the case of protons, we observe a crossing of curves for $v \sim 5$, an effect that will be discussed later. In all the cases, the high-energy decline of the stopping power is consistent with the asymptotic Bethe-like behavior [13]. At impact velocities lower than 5 a.u. a clear change of behavior for all projectiles can be noted. Also, a seeming anomalous behavior

of the stopping power can be observed in Fig. 8 for electrons and positrons in the range of subthermal projectile velocities. This is an interesting result of the effects of thermal fluctuations in the energy exchanges, which take place in the range of subthermal energies [$E < (3/2)k_BT$], where the particles receive energy from the plasma, leading on average to negative energy losses [13]. Additionally, the image of well-defined particle trajectories is lost in this region, as is also the ideal concept of stopping power of light particles with small velocities moving along straight trajectories. In this case, a more appropriate magnitude to characterize the slowing down process is the mean energy loss or gain per unit time, $d\overline{E}/dt$. In particular, for positrons in the limit $v = 0$, it may be shown that this quantity has a well-defined negative-limit value given by

$$-\frac{d\overline{E}}{dt} = -v\frac{d\overline{E}}{dx}$$
$$= -\frac{2e^2\hbar}{\pi m}\int_0^\infty q^2 N(\gamma\, q^2)\, \text{Im}\left[\frac{-1}{\varepsilon(q, \gamma q^2)}\right]dq \quad (20)$$

with $\gamma = \hbar/2m$. Similarly, finite values at $v = 0$ can be obtained for the average collision time $\tau = \Lambda/v$, and for the energy straggling per unit time, $v\Omega^2 = \langle\Delta E^2\rangle/\Delta t$.

Another question that arises in the case of positrons is the possibility of annihilation by a contact interaction with target electrons [15]. However, the positron annihilation lifetime is usually significantly larger than the slowing down time [16]; therefore, this process does not affect the present considerations. Moreover, when dealing with very small speeds, an additional energy-loss channel must be considered: interactions with plasma ions [79,80]. The description of these processes lies beyond the scope of the present work, devoted to electronic excitations, and would require a separate study.

Finally, we remark on the excellent agreement of the results obtained by these two different and independent approaches
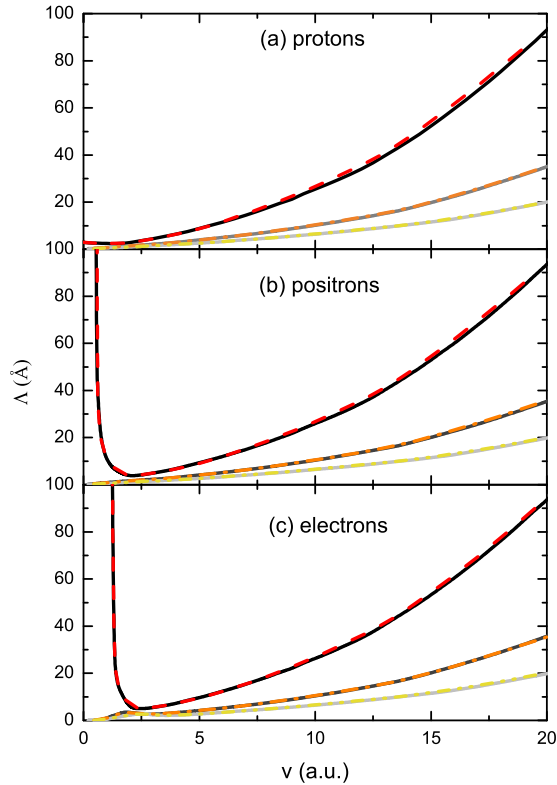
FIG. 11. Mean-free path Λ of different projectiles traversing a Si solid-state-density plasma as a function of projectile velocity for the three temperatures indicated in Fig. 8, for (a) protons, (b) positrons, and (c) electrons. Curves: as in Fig. 8, with temperatures $T = 0$ (upper curves), 30 (middle curves), and 60 eV (lower curves).
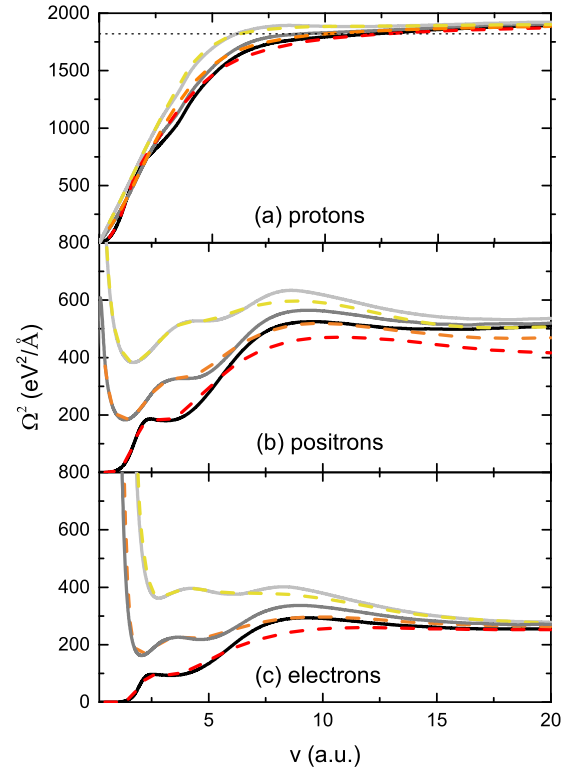

FIG. 12. Straggling of different projectiles traversing a Si solid-state-density plasma as a function of projectile velocity for the three temperatures indicated in Fig. 8, for impinging (a) protons, dotted line, Bohr's value; (b) positrons; and (c) electrons. Curves: as in Fig. 8.

(UWPM and SLPA) at all the temperatures and for the three particles considered, as shown in Fig. 8.

With regard to heavy particles, the range of main interest for the interaction of energetic ions with plasmas—such as heating by external ion beams or internally produced 3.5-MeV alpha particles—is primarily well above the range of thermal energies, i.e., the case of high-impact energies. This leads us to consider the region of curves crossing observed in Fig. 8. To magnify this region and appreciate the temperature dependence, we display in Fig. 9 the ratios of the stopping power relative to the corresponding values for zero temperature, namely, $S(v, T)/S(v, 0)$, obtained with the UWPM and SLPA, for temperatures of 30 and 60 eV. This figure shows the stopping ratios in a way that the behavior for velocities greater than 5 a.u. can be clearly appreciated. In this velocity range, an increase of the stopping power with increasing temperature is observed, not only for protons, as it has been previously shown in Ref. [12], but also for light particles: positrons and electrons. Both approaches, UWPM and SLPA, verify the result shown here. Thus, we find that the special restrictions that apply to light particles do not modify the effect of thermal enhancement of the stopping in the range of intermediate energies; it is important to mention that this effect was experimentally observed using proton beams in Ref. [81].

However, at lower energies, this effect is reversed (i.e., the stopping ratios fall below 1), as it is clearly shown in

Fig. 10. This figure is focused on the stopping ratios for the case of protons in the same range of velocities, showing the FEG and inner-shell ratios in separate curves. To ease the identification, the letters t, t′, and t″ attached to the curves in Fig. 10 correspond to the total stopping ratios for temperatures 30, 60, and 200 eV, and similar notations are used for the free electron (f) and inner-shell (i) components. Here we clearly appreciate that the increase of the total stopping power ratios with temperature, from t to t′, and from t′ to t″, is due to the increase of electron density in the FEG, whose contributions increase from f to f′ and from f″ to f″, as a result of the thermal ionization process, while the reduction of the number of bound electrons diminishes the inner shell contributions from i to i′, and from i′ to i″, producing the inverse effect in these contributions, as shown by the red curves. We can also observe the behavior change in the total ratios for low velocities, where their values drop below 1. This obeys the same behavior change of the FEG ratios, which fully dominates the stopping power in this velocity region. This inversion of the behavior for low velocities can be explained by the relaxation of the dielectric energy-loss function with temperature [6]. So, even when the ionization increases the electron density of the plasma, it does not compensate for the decrease produced by the thermal relaxation of the dielectric response, which affects the velocity region below and around the stopping maximum (cf. Fig. 8).

Thus, the behavior of the dielectric response produces a curious effect: a decrease of the stopping power with

increasing temperatures at low velocities and a mild increase for intermediate velocities.

Furthermore, for intermediate and high velocities, Fig. 10 shows an increase in the stopping power, as can be observed when going from curves t′ to t″. However, this stopping enhancement is a particular effect resulting from a competition of temperature and velocity dependencies, and its outcome may reverse if different conditions are set. A more complete characterization of this effect requires a more detailed analysis, which is given in the Appendix.

Figure 11 shows the velocity and temperature dependency of the results for the mean-free path Λ. Here, by comparing the results for light particles and protons, we find important differences in the low-velocity region, produced not only by the special restrictions for light particles already indicated but also due to statistical effects related to the Bose terms $N(\omega')$ that appear in the treatment of the plasma excitations; these terms regulate the contributions of gain and loss processes, and dominate the behavior in the case of light particles and low energies. The effects produced by these terms have been described in detail in Ref. [13] for the case of a pure FEG and appear again here, in the more general context of a plasma containing bound and free electrons, because the free-electron component dominates the behavior at low velocities.

The striking effect that we find here [Figs. 11(b) and 11(c)] is the sudden increase of Λ at low energies for the case $T = 0$, a diverging effect that disappears for the cases $T = 30$ and $T = 60$. The cause of this behavior is that the inverse mean-free path, Λ^{-1}, goes to zero at $v \sim 0$ for positrons and at $v \sim v_F$ for a FEG, as shown much earlier by Ritchie [18]; therefore, in these limits, the mean-free path Λ shows a divergent behavior. This also explains the shift in the point of divergence of the curves for these two particles when $T = 0$. For finite temperatures, there are thermal excitations in the plasmas, described by the statistical factor $N(\omega)$, Eq. (13). These excitations dominate the behavior for small frequency values ($\omega < k_B T$), so when the energy of the particle approaches $k_B T$, these excitations produce a growing number of low-energy exchange events (gain and loss processes) between the particle and the plasma, and as a consequence the mean-free path for these interactions decreases and tends to zero at $v \sim 0$.

The second relevant effect that we find in Fig. 11 is the important decline of the mean-free path values with increasing temperatures. This effect can be seen, in alternative terms, as a significant increase in the values of Λ^{-1}, and is also larger than the increase already observed in the stopping power in Fig. 9. In quantitative terms, the decreases in the values of Λ are around 45%–60% for intermediate and high velocities, whereas the increases of the stopping powers shown in Fig. 9 are around 10%–15%. A closer examination of this effect shows that the decline in the Λ values is also produced by the statistical factors $N(\omega)$, i.e., the effect of the interactions with the background of thermal excitations.

Finally, Fig. 12 shows the results of the energy straggling Ω^2 for protons, positrons, and electrons for Si at $T = 0$ eV, $T = 30$ eV, and $T = 60$ eV. We find in this case that the effects of the temperature become much more significant for the light particles than for protons. Here the increase in the temperature produces a rather minor increase in the straggling values for

protons and a very large enhancement in the cases of positrons and electrons. Again, this may be shown to be produced by the behavior of the free electrons in the plasma, through the factors $N(\omega')$, according to the formulation given in Sec. III. In the low-energy range, the energy straggling is dominated by loss and gain processes arising from thermal excitations of the medium, which produce large energy-loss fluctuations. As could be expected, the effects of these fluctuations are clearly seen in the energy straggling. The divergent type of behavior of the positron and electron straggling at low energies is also produced by this thermal fluctuation; we can also see here the shift in the point of divergence, located at $v \sim 0$ for positrons and at $v \sim v_F$ for electrons. Pronounced shoulders in the straggling curves can also be observed for the light particles (very much attenuated for protons) at low and intermediate velocities. These shoulders soften slightly when the temperature increases. The increasing depopulation of inner shells with temperature can explain this. The first shoulder is caused by the FEG contribution, and the inner-shell contributions produce the others.

For further or more detailed considerations regarding the role of gain and loss processes in the energy-loss moments of particles in a FEG, we refer to the extensive discussion given in Ref. [13] (see in particular Fig. 11 of this reference, where the contributions of loss and gain terms are shown separately).

Finally, we wish to stress that, apart from some minor differences, there is a remarkable agreement between the results of these two different approaches (UWPM and SLPA) as shown by the previous figures.

V. SUMMARY AND CONCLUSIONS

As indicated in the Introduction, the purpose of this work was to apply and compare two dielectric methods (UWPM and SLPA) for studying the interaction of test particles with cold targets and quantum plasmas in thermal equilibrium conditions.

To this end, we extended the UWPM and SLPA formulations of the interaction process developed in previous works, and we made a comprehensive study of inner-shell and thermal effects, considering the cases of heavy and light particles, and performing a set of calculations of the three most relevant ELMs, namely, stopping power, energy-loss straggling, and inelastic mean-free path. We analyzed a set of cases of interest for current fusion projects and astrophysical studies, and we compared them with experimental results in the case of cold targets, obtaining satisfactory agreements.

On one side, the results for the stopping power of protons in three different targets (Si, Al, and Fe) are consistent with previous calculations [12]. But the subject of interest here was to extend the study to all cases (light and heavy projectiles) and to include the contribution of bound and free electrons on a fully consistent basis, with the aim to obtain knowledge and explore possible differences or similarities between both methods. With this purpose, a set of new results were obtained, and detailed comparisons between the different types of interacting particles were made, paying special attention to the physical origin of new effects.

Comparative studies of the ELMs, showing the contribution of free and bound electrons, were analyzed in Figs. 1–3.

Among the new effects, we have discussed with much detail the influence of inner-shell electrons on the three ELMs for a cold Si target, comparing the results for the different projectiles. We found a faster decline of the FEG contributions in the case of protons compared to the cases of positrons and electrons (Fig. 4). This effect may be explained by the additional kinematic and quantum restrictions applied to light particles. Similar conclusions may be obtained for Al and Fe.

For Al targets, we find that the stopping power for high-velocity positrons is around 14%–25% higher than those for electron impact (Fig. 6). This effect is explained by the additional quantum restrictions for electrons and compares well with the percentage of 15% obtained experimentally [34,35].

In a further development, we have studied temperature effects on the ELMs for the three types of particles. A detailed study was made through the analysis of stopping ratios for a Si target; this shows that the reason for the increasing behavior of stopping power with the temperature at relatively large velocities is the target ionization: new ionized electrons increase the FEG electron density and consequently the stopping power, producing a stopping enhancement effect. This effect is also in agreement with the experimental results reported in Ref. [81].

In the case of low velocities, the increase of the ionization does not compensate for the reduction of stopping produced by the decreasing behavior of the energy-loss function when the temperature increases (cf. Ref. [6]), and consequently, the tendency inverts: the higher the temperature, the lower the maxima of the stopping curves. This produces an interesting competition between increasing the density of free electrons (by thermal ionization) and decreasing the energy absorption efficiency of those electrons.

We extended the analysis of thermal ionization considering temperatures up to 1000 eV (see the Appendix), and we show that when almost all the inner shells are depopulated, the probability of further ionization is exhausted. The dominant behavior of the electron gas takes over. This leads to a final decline of the stopping power at higher temperatures, which reverses the enhancement effect mentioned previously. Therefore, another interesting conclusion of this study is that the experimentally observed enhancement of the stopping power (Ref. [81]) will be reversed if further experiments are performed in the future at still higher temperatures.

We have also analyzed the mean-free path and energy-straggling values for protons traversing hot targets, observing a decreasing behavior for the Λ and an increasing behavior for the straggling when the temperature increases (Figs. 11 and 12). The Λ shows a more substantial effect on the temperature than the stopping power due to the dominant contribution of the FEG and the background of thermal excitations. However, the energy straggling of protons is not very much affected by thermal effects (Fig. 12).

In the case of electrons and positrons, significant differences concerning protons were found. At large energies, the results for the stopping power of these particles show an increase in temperature similar to the case of protons, but for energies around or below the maximum, a dramatic drop in the stopping values is found, turning to negative values in the range of subthermal speeds (Figs. 8 and 9). The mean-free path and straggling results for these light particles also show a very striking behavior (Figs. 11 and 12): for zero temperature
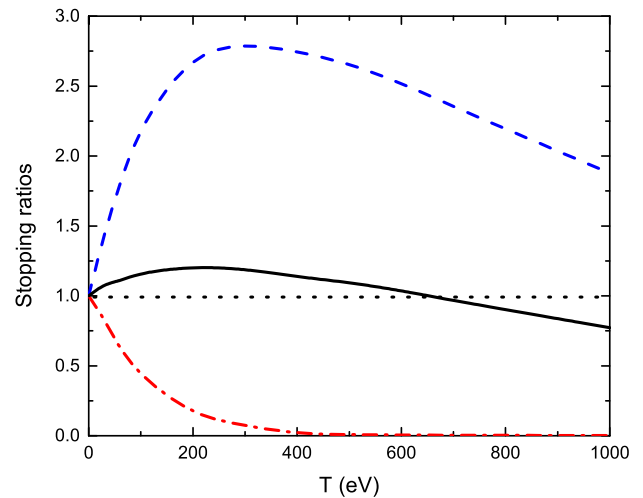

FIG. 13. Stopping power ratios concerning cold target values for Si solid-state-density plasma as a function of temperature. Black solid line, total ratio; Blue dashed line, FEG; red dashed-dotted line, inner shells.

and low velocities, the Λ shows a divergent behavior while the straggling tends to zero (this is the known "normal" behavior in accord with previous works); however, when the temperature increases the Λ values drop to zero, and the straggling values diverge (always in the range of low velocities). These seeming anomalies are produced by the growing role of thermal fluctuations that affect the behavior of light particles very strongly. Additionally, the contribution of inner shells (when populated) has a significant increase in the straggling values and shoulders in the case of electrons and positrons (Fig. 12).

Finally, we wish to note the consistency and excellent agreement found in most cases between two dielectric approaches, given by the UWPM and the SLPA, to represent the interaction of heavy and light particles with dense plasmas,
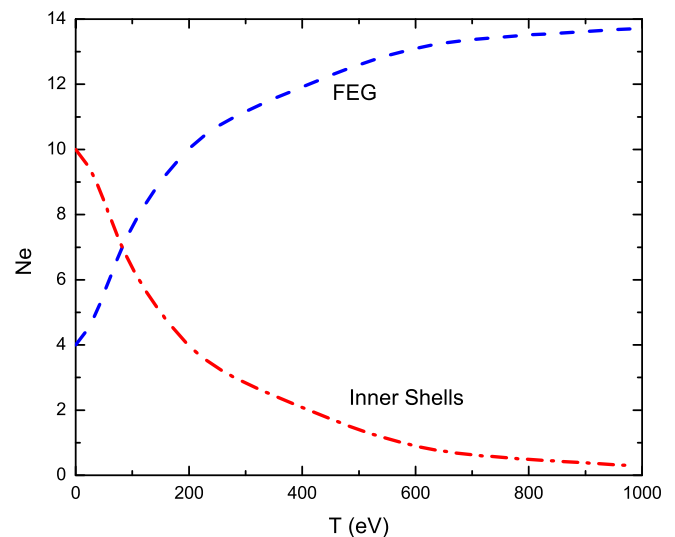

FIG. 14. Ionization for a Si solid-state-density plasma as a function of temperature. Blue dashed line, FEG; red dashed-dotted line, inner shells.
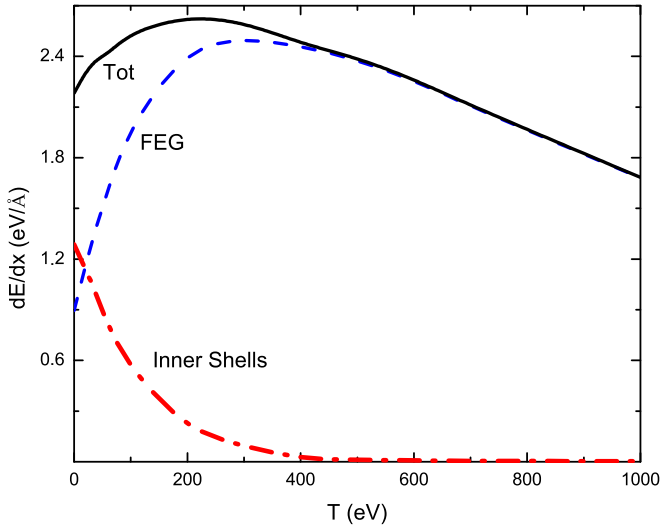
FIG. 15. Stopping power of protons traversing a Si solid-state-density plasma as a function of temperatures for a projectile velocity $v = 10$ a.u. Black solid line, total; blue dashed line, FEG; red dashed-dotted line, inner shells.

including the contributions of bound and free electrons in the system. Extending the present study to the case of dilute plasmas would be relatively straightforward.

The most significant difference between the SLPA and the UWPM methods is that the former takes into account in a direct way the values of the electron density of all the target shells, whereas the UWPM treatment works in the momentum space, taking into account the Hartree-Fock results for the velocity distributions of each shell, and where the inhomogeneities of the electron densities are indirectly represented in the Fourier space. On the other hand, the UWPM method allows a more adequate description of temperature effects as compared with the SLPA, whose dielectric response for the atomic shells is based on Lindhard's model for a degenerate electron gas (accounting for binding effects through the Levine-Louie method).

Remarkably, despite these intrinsic differences, the results we obtained with both approaches are in very good agreement, being almost identical in some cases. This provides confidence in the consistency of both approaches to describe interaction processes between charged particles and dense or dilute plasmas.

As a general conclusion, we think these results present an alternative way to calculate interaction processes in plasmas on an extensive range of plasma conditions, including those systems of current interest in fusion research and other types of plasma cases of astrophysical interest.

APPENDIX: THE EFFECTS OF TARGET IONIZATION BY TEMPERATURE

This Appendix provides a complete analysis of the so-called stopping enhancement effect obtained in Sec. IV C, which corresponds with the experimental results reported in Ref. [81]. A complete study covering higher temperatures shows that this enhancement of the stopping power is followed by a decline at higher temperatures, which is produced by the particular behavior of the free plasma electrons. Hence, to get further insight, we wish to expand here the previous analysis to obtain a complete picture of this phenomenon and to explain the physical origin of this rather complex behavior.

A convenient way to show the effects of temperature on the stopping power due to the target ionization is to analyze the behavior for a fixed proton velocity. Here we choose $v = 10$ a.u., which corresponds to the range of velocities where a stopping enhancement was obtained, as shown in Fig. 9. For this particular study, we consider the UWPM approach.

Extending the analysis given in the text, we define the *stopping power ratios* corresponding to the FEG and the IS, given by

$$S_{\text{FEG}}(v, T)/S_{\text{FEG}}(v, 0) \tag{A1}$$

and

$$S_{\text{IS}}(v, T)/S_{\text{IS}}(v, 0), \tag{A2}$$

respectively, and the total stopping ratio,

$$S_{\text{total}}(v, T)/S_{\text{total}}(v, 0), \tag{A3}$$

relative to the corresponding values for a cold silicon target ($T = 0$).

We show in Fig. 13 the partial and total stopping power ratios as a function of the target temperature for the particular case $v = 10$ a.u. Here we see that, in contrast with the significant variations of the FEG and IS ratios, the total stopping ratio has a mild increase for temperatures below 200 eV, reaching a maximum (where the stopping for that temperature is about 20% higher than the stopping for a cold target) followed by a decline at higher temperatures. This is the soft enhancement effect depicted in Fig. 9 for intermediate temperatures and is a result of two competing effects: the ionization process that sends electrons to the FEG and the declining dependency of the energy-loss function, $\text{Im}[-1/\varepsilon(q, \omega)]$ (which determines the FEG stopping power), with temperature [6]. Hence, the new feature that this figure shows is the final decline of the stopping ratio for higher temperatures, where the FEG entirely dominates the stopping process.

To understand these surprising results, we must perform a more in-depth analysis of the effects of thermal ionization. Figure 14 shows the impact of inner-shell ionization according to the results of the FLYCHK code [46] for a Si target with average solid-state density $n = 2.33$ g/cm^3. This figure shows how thermal ionization progressively depopulates the inner shells, transferring electrons to the FEG. We notice that starting from four valence electrons and after a substantial increase up to around 400 eV, the FEG curve slowly converges asymptotically to the total number of 14

electrons. For temperatures over 700 eV, the target is almost completely ionized, leaving less than 0.5 electrons in the $1s$ shell.

Figure 15 shows the contributions to the stopping power due to the FEG and IS, as well as the total stopping power, also for protons with velocity $v = 10$ a.u. Here we can verify that the rapid variations of the FEG and IS contributions

are produced by the ionization effect shown in Fig. 14. For temperatures over about 400 eV, almost all the stopping power is produced by the free plasma electrons. Therefore, the final decrease of the total stopping ratio shown in Fig. 13 is produced by the behavior of the free-electron stopping power as the temperature increases. This decrease is typical of the free electron gas (see, e.g., Ref. [5]).

---

[1] S. Putvinski, W. Heidbrink, G. Martin, F. Porcelli, F. Romanelli, G. Sadler, K. Tobita, J. W. Van Dam, and S. Zweben, Alpha-particle physics in Tokamaks, Phil. Trans. R. Soc. Lond. A **357**, 493 (1999).

[2] K. A. Long and N. A. Tahir, Theory and calculation of the energy loss of charged particles in inertial confinement fusion burning plasmas, Nucl. Fusion **26**, 555 (1986).

[3] C. J. Hansen, S. D. Kawaler, and V. Trimble, *Stellar Interiors* (Springer-Verlag, New York, 2004).

[4] N. R. Arista and W. Brandt, Energy loss and straggling of charged particles in plasmas of all degeneracies, Phys. Rev. A **23**, 1898 (1981).

[5] G. Maynard and C. Deutsch, Energy loss and straggling of ions with any velocity in dense plasmas at any temperature, Phys. Rev. A **26**, 665 (1982).

[6] N. R. Arista and W. Brandt, Dielectric response of quantum plasmas in thermal equilibrium, Phys. Rev. A **29**, 1471 (1984).

[7] L. de Ferrariis and N. R. Arista, Classical and quantum mechanical treatments of the energy loss of charged particles in dilute plasmas, Phys. Rev. A **29**, 2145 (1984).

[8] M. D. Barriga-Carrasco, F. Chacón-Rubio, and C. C. Montanari, Stopping power of plasma free and bound electrons using dielectric formalism, Eur. Phys. J. Plus **137**, 375 (2022).

[9] M. D. Barriga-Carrasco, Heavy ions charge-state distribution effects on energy loss in plasmas, Phys. Rev. E **88**, 043107 (2013).

[10] C. F. Clauser and N. R. Arista, Stopping power of dense plasmas, Phys. Rev. E **97**, 023202 (2018).

[11] L. González-Gallego, M. D. Barriga-Carrasco, and J. Vázquez-Moyano, Reduced stopping power of protons propagatin through hot plasmas, Phys. Plasmas **28**, 043103 (2021).

[12] C. D. Archubi and N. R. Arista, Unified description of interactions and energy loss of particles in dense matter and plasmas, Phys. Rev. A **102**, 052811 (2020).

[13] C. D. Archubi and N. R. Arista, General formulation of interactions and energy loss of particles in plasmas: Quantum-wave-packet model versus a semiclassical approach, Phys. Rev. A **105**, 032806 (2022).

[14] *Interaction of Positrons with Matter and Radiation*, edited by A. K. Bhatia (MDPI Press, Basel, 2021).

[15] W. Brandt, Positrons as a probe of the solid state, Sci. Am. **233**, 34 (1975).

[16] P. J. Schultz and K. G. Lynn, Interaction od positron beams with surfaces, thin films and interfaces, Rev. Mod. Phys. **60**, 701 (1988).

[17] M. J. Puska and R. M. Nieminen, Theory of positrons in solids and on solid surfaces, Rev. Mod. Phys. **66**, 841 (1994).

[18] R. H. Ritchie, Interaction of charged particles with a degenerate Fermi-Dirac electron gas, Phys. Rev. **114**, 644 (1959).

[19] F. W. Garber, J. A. Harter, R. D. Birkhoff, and R. H. Ritchie, Oak Ridge National Laboratory Report No. ORNL-TM-2406 (1969); F. W. Garber, M. Y. Nakai, J. A. Harter, and R. D. Birkhoff, Low energy electron beam studies in thin aluminum foils, J. Appl. Phys. **42**, 1149 (1971).

[20] J. R. Young, Penetration of electrons in aluminum oxyde films, Phys. Rev. **103**, 292 (1956).

[21] H. J. Fitting, Transmission, energy distribution, and SE excitation of fast electrons in thin solid films, Phys. Status Solidi A **26**, 525 (1974).

[22] K. O. Al-Ahmad and D. E. Watt, Stopping powers and extrapolated ranges for electrons (1–10 keV) in metals, J. Phys. D: Appl. Phys. **16**, 2257 (1983).

[23] M. P. Seah, Quantitative Auger electron spectroscopy and electron ranges, Surf. Sci. **32**, 703 (1972).

[24] D. T. Pierce and W. Spicer, Electronic structure of amorphous Si from photoemission and optical studies, Phys. Rev. B **5**, 3017 (1972).

[25] M. Klasson, A. Berndtsson, J. Hedman, R. Nilsson, R. Nyholm, and C. Nordling, Electron escape depth in silicon, J. Electron Spectrosc. Relat. Phenom. **3**, 427 (1974).

[26] V. I. Zaporozhchenko, Y. D. Kalafati, Y. A. Kukharenko, and V. M. Sergeev, Izv. Akad Nauk SSSR. Ser. Fiz. **43**, 1919 (1979).

[27] D. C. Joy, S. Luo, R. Gauvin, P. Hovington, and N. Evans, Experimental measurements of electron stopping power at low energies, Scanning Microsc. **10**, 4 (1996).

[28] C. J. Powell and A. Jablonsky, Evaluation of calculated and measured electron inelastic mean-free paths near solid surfaces, J. Phys. Chem. Ref. Data **28**, 19 (1999).

[29] W. S. M. Werner, T. Tomastik, T. Cabela, G. Richter, and H. Störi, Electron inelastic mean-free path measured by elastic peak electron spectroscopy for 24 solids between 50 and 3400 eV, Surf. Sci. **470**, L123 (2000).

[30] S. Tanuma, T. Shiratori, T. Kimura, K. Goto, S. Ichimura, and C. J. Powell, Experimental determination of electron inelastic mean free paths in 13 elemental solids in the 50 to 5000 eV energy range by elastic-peak electron spectroscopy, Surf. Interface Anal. **37**, 833 (2005).

[31] B. Yang, C.-K. Ng, C.-C. Lin, and S. Fung, Energy loss of monoenergetic positrons passing through a thin carbon foil, Nucl. Instrum. Methods Phys. Res., Sect. B **270**, 9 (2012).

[32] J. A. Baker, N. E. Chilton, and P. G. Coleman, Stopping of 10–50 keV positrons in aluminum, Appl. Phys. Lett. **59**, 164 (1991).

[33] W. N. Lennard, P. J. Schultz, G. R. Massoumi, and L. R. Logan, Observation of the Difference between $e^- - e^-$ and $e^+ - e^-$ Interactions, Phys. Rev. Lett. **61**, 2428 (1988).

[34] P. J. Schultz, L. R. Logan, W. N. Lennard, and G. R. Massoumi, Slowing down of positrons in solids, AIP Conf. Proc. **205**, 639 (1990).

[35] W. N. Lennard, G. R. Massoumi, P. J. Schultz, P. J. Simpson, and G. C. Aers, Stopping Powers for Positrons and Electrons, Phys. Rev. Lett. **74**, 3947 (1995).

[36] H. Bethe, Zur theorie des durchgangs schneller korpusku-larstrahlen durch materie, Ann. Phys. **397**, 325 (1930).

[37] J. Lindhard, On the properties of a gas of charged particles, Mat. Fys. Medd. Dan. Vid. Selsk **28**, 1 (1954); J. Lindhard and A. Winther, Stopping power of electron gas and equipartition rule, **34**, 1 (1964).

[38] J. C. Ashley, Interaction of low-energy electrons with condensed matter: Stopping powers and inelastic mean-free paths from optical data, J. Electron Spectrosc. Relat. Phenom. **46**, 199 (1988).

[39] J. M. Fernández-Varea, R. Mayol, D. Liljequist, and F. Salvat, Inelastic scattering of electrons in solids from a generalized oscillator strength model using optical and photoelectric data, J. Phys.: Condens. Matter **5**, 3593 (1993).

[40] R. García-Molina, I. Abril, I. Kyriakou, and D. Emfietzoglou, Inelastic scattering and energy loss of swift electron beams in biologically relevant materials, Surf. Interface Anal. **49**, 11 (2017).

[41] P. de Vera and R. García-Molina, Electron inelastic mean free paths in condensed matter down to a few electronvolts, J. Phys. Chem. C **123**, 2075 (2019).

[42] T. Kaneko, Wave packet theory of bond electrons, Phys. Rev. A **40**, 2188 (1989).

[43] T. Kaneko, Partial and total electronic stoppings of solids and atoms for energetic ions, Phys. Status Solidi B **156**, 49 (1989).

[44] T. Kaneko, Partial and total electronic stopping cross sections of atoms and solids for protons, At. Data Nucl. Data Tables **53**, 271 (1993).

[45] C. D. Archubi and N. R. Arista, Extended wave-packet model to calculate energy-loss moments of protons in matter, Phys. Rev. A **96**, 062701 (2017).

[46] H. K. Chung, M. H. Chen, W. L. Morgan, Y. Ralchenko, and R. W. Lee, FLYCHK: Generalized population kinetics and spectral model for rapid spectroscopic analysis for all elements, High Energy Density Phys. **1**, 3 (2005).

[47] V. I. Ochkur, Soviet Phys. J. E. T. P. **47**, 1766 (1964).

[48] B. H. Bransden, Atomic collision theory, in *Lecture Notes and Supplements in Physics*, Mathematics Lecture Note Series, edited by W. A. Benjamin (1970), Vol. 12.

[49] R. Hippler and W. Jitschin, Plane wave Born cross sections including exchange for K-shell ionization of light atoms, Z. Phys. A **307**, 287 (1982).

[50] H. Shinotsuka, S. Tanuma, C. J. Powell, and D. R. Penn, Calculations of electron stopping powers for 41 elemental solids over the 50 eV to 30 keV range with the full Penn algorithm, Nucl. Instrum. Methods Phys. Res., Sect. B **270**, 75 (2012).

[51] H. A. Bethe and J. Ashkin, Passage of radiation through matter, in *Experimental Nuclear Physics*, edited by E. Segré (Wiley, New York, 1953).

[52] L. D. Landau and E. M. Lifshitz, *Quantum Mechanics: Non-Relativistic Theory*, 2nd ed. (Pergamon Press, New York, 1977), p. 637.

[53] C. C. Montanari and J. E. Miraglia, The dielectric formalism for inelastic processes in high-energy ion-matter collisions, Adv. Quant. Chem. **65**, 165 (2013).

[54] C. D. Archubi, C. C. Montanari, and J. E. Miraglia, Many-electron model for multiple ionization in atomic collisions, J. Phys. B: At. Mol. Opt. Phys. **40**, 943 (2007).

[55] C. C. Montanari and J. E. Miraglia, Stopping power of protons in transition metals of the groups V and VI, Nucl. Instrum. Methods Phys. Res., Sect. B **460**, 27 (2019).

[56] J. P. Peralta, M. Fiori, A. M. P. Mendez, and C. C. Montanari, Stopping-power calculations and the Levine-Mermin dielectric function for inner shells, Phys. Rev. A **105**, 062814 (2022).

[57] Z. H. Levine and S. G. Louie, New model dielectric function and exchange-correlation potential for semiconductors and insulators, Phys. Rev. B **25**, 6310 (1982).

[58] D. Pines, Classical and quantum plasmas, Plasma Phys. **2**, 5 (1961).

[59] E. M. Bringa and N. R. Arista, Energy loss of correlated ions in plasmas: Collective and individual contributions, Phys. Rev. E **54**, 4101 (1996).

[60] P. M. Platzman and P. A. Wolff, *Elementary Excitations in Solid-State Plasmas* (Academic Press, New York, 1973).

[61] C. D. Archubi and N. R. Arista, A comparative study of threshold effects in the energy loss moments of protons, electrons, and positrons using dielectric models for band gap materials, Eur. Phys. J. B **90**, 18 (2017).

[62] *Electronic Stopping Power of Matter for Ions, Graphs, Data, Comments and Programs*, https://www-nds.iaea.org/stopping/; C. C. Montanari and P. Dimitriou, The IAEA stopping power database, following the trends in stopping power of ions in matter, Nucl. Instrum. Methods Phys. Res., Sect. B **408**, 50 (2017).

[63] G. Hobler, K. K. Bourdelle, and T. Akatsu, Random and channeling stopping power of H in Si below 100 keV, Nucl. Instrum. Methods Phys. Res., Sect. B **242**, 617 (2006).

[64] M. Abdesselam, S. Ouichaoui, M. Azzouz, A. C. Chami, and M. Siad, Stopping of 0.3–1.2 MeV/u protons and alpha particles in Si, Nucl. Instrum. Methods Phys. Res., Sect. B **266**, 3899 (2008).

[65] M. Brocklebank, S. N. Dedyulin, and L. V. Goncharova, Stopping cross sections of protons in Ti, TiO_2 and Si using medium energy ion scattering, Eur. Phys. J. D **70**, 248 (2016).

[66] C. Tschalär and H. Bichsel, Mean excitation potential of light compounds, Phys. Rev. **175**, 476 (1968).

[67] J. D. Mewins and T. A. Tombrello, Energy loss of low energy protons channeling in silicon crystals, Radiat. Eff. **26**, 113 (1975).

[68] C. J. Tung, J. C. Ashley, and R. H. Ritchie, Electron inelastic mean-free paths and energy losses in solids II: Electron gas statistical model, Surf. Sci. **81**, 427 (1979).

[69] M. J. Berger *et al.*, Electron collision stopping powers at low energies, J. ICRU **os19**, 39 (1984).

[70] W. M. Ariyasinghe, H. T. Awuku, and D. Powers, L-shell ionization of Si, P, S, Cl, and Ar by 0.4- to 2.0-MeV H^+ and 0.4- to 1.2-Mev H^{2+} bombardment, Phys. Rev. A **42**, 3819 (1990).

[71] J. J. Vrakking and F. Meyer, Electron-impact-ionization cross sections of inner shells measured by Auger-electron spectroscopy, Phys. Rev. A **9**, 1932 (1974).

[72] G. Konac, S. Kalbitzer, Ch. Klatt, D. Niemann, and R. Stoll, Energy loss and straggling of H and He ions of keV energies in Si and C, Nucl. Instrum. Methods Phys. Res., Sect. B **136-138**, 159 (1998).

[73] D. G. Arbó, M. S. Gravielle, J. E. Miraglia, J. C. Eckardt, G. H. Lantschner, M. Famá, and N. R. Arista, Energy straggling of protons through thin solid foils, Phys. Rev. A **65**, 042901 (2002).

[74] A. Ikeda, K. Sumimoto, T. Nishiola, and Y. Kido, Stopping powers and energy straggling for 50–300 keV H$^+$ in amorphous Si and Ge films, Nucl. Instrum. Methods Phys. Res., Sect. B **115**, 34 (1996).

[75] Y. Kido, Energy straggling for fast proton beams passing through solid materials, Nucl. Instrum. Methods Phys. Res., Sect. B **24-25**, 347 (1987).

[76] D. W. Moon, H. I. Le, K. J. Kim, T. Nishimura, and Y. Kido, Estimation of the electronic straggling using delta-doped multilayers, Nucl. Instrum. Methods Phys. Res., Sect. B **183**, 10 (2001).

[77] C. C. Montanari, J. E. Miraglia, S. Heredia-Avalos, R. Garcia-Molina, and I. Abril, Calculation of energy-loss straggling of C, Al, Si, and Cu for fast H, He, and Li ions, Phys. Rev. A **75**, 022903 (2007).

[78] C. C. Montanari and J. E. Miraglia, The energy loss straggling of low Z ions in solids and gases, AIP Conf. Proc. **1525**, 259 (2013).

[79] S. T. Butler and M. J. Buckinham, Energy loss of a fast ion in a plasma, Phys. Rev. **126**, 1 (1962).

[80] A. G. Sitenko, *Electromagnetic Fluctuations in a Plasma* (Academic Press, New York, 1967).

[81] F. C. Young, D. Mosher, S. J. Stephanakis, S. A. Goldstein, and T. A. Mehlhorn, Measurements of Enhanced Stopping of 1-MeV Deuterons in Target-Ablation Plasmas, Phys. Rev. Lett. **49**, 549 (1982).